Switching induced by spin Hall effect in an in-plane magnetized ferromagnet with the easy axis parallel to the current

Tomohiro Taniguchi ⬢
*National Institute of Advanced Industrial Science and Technology (AIST), Spintronics Research Center,
Tsukuba, Ibaraki 305-8568, Japan*

Magnetization switching in a fine-structured ferromagnet of nanoscale by the spin-transfer torque excited via the spin Hall effect has attracted much attention because it enables us to manipulate the magnetization without directly applying current to the ferromagnet. However, the switching mechanism is still unclear in regard to the ferromagnet having an in-plane easy axis parallel to the current. Here we develop an analytical theory of the magnetization switching in this type of ferromagnet, and reveal the threshold current formulas for a deterministic switching. It is clarified that the current should be in between a certain range determined by two threshold currents because the spin-transfer torque due to a large current outside the range brings the magnetization in an energetically unstable state, and causes magnetization precession around the hard axis.

I. INTRODUCTION

Spin-orbit interaction in a nonmagnetic metal scatters conducting electrons in a direction perpendicular to both current and spin angular momentum. Spin Hall effect is a physical phenomenon generating pure spin current via such spin-orbit interaction [1–3]. Attaching a ferromagnet to the nonmagnet, the pure spin current injected into the ferromagnet excites spin-transfer torque [4,5] and induces magnetization dynamics such as switching and auto-oscillation [6–18]. These magnetization dynamics have gained much attention from viewpoints of both fundamental and applied physics because these dynamics are interesting examples of nonlinear phenomena in nanoscale [19], and can be used for practical devices such as three-terminal magnetic random access memory [20].

The physical systems related to the spin Hall effect are classified into three different types. The first one is the system with a ferromagnet having an in-plane easy axis orthogonal to the current direction [6,8,9] named as type Y in Ref. [18]. In this case, the spin polarization of the spin current is parallel to the easy axis. The theoretical analysis for the system is well developed because the system is similar to two-terminal magnetic multilayers proposed for the original concept of the spin-transfer torque [4,5,21–25], where the magnetization dynamics is excited as a result of the competition between the spin-transfer torque and the damping torque. The second one is the system with a ferromagnet having a perpendicular easy axis [7,8,10–17,26,27], named as type Z [18]. The magnetization switching in this system has been extensively studied [28–34], particularly due to its applicability to practical devices. The third one is the system with a ferromagnet having the easy axis parallel to the current direction, named as type X [18]. This system is easy to fabricate, and a small cross-section area for the current injection is also preferable for practical purposes. In addition, it was shown that the

system is able to achieve a fast magnetization switching [18]. Despite these fascinating properties, however, the physical mechanism of the magnetization switching in this system has not been investigated yet, which prevents us from establishing a comprehensive dynamical theory of the magnetization.

The purpose of this work is to develop theoretical formulas of the magnetization switching caused by the spin Hall effect in the ferromagnet having the easy axis parallel to the current. Solving the Landau-Lifshitz-Gilbert (LLG) equation numerically, phase diagrams clarifying the magnetization state in a steady state are obtained. An analytical formula is derived for the critical current inducing the magnetization switching, showing good agreement with the phase diagram. The magnetization state after turning off the current is also investigated. The numerical simulation reveals the existence of another threshold value of the current for the switching, i.e., a deterministic switching can be achieved when the current is in between a range determined by two threshold currents. An analytical formula for this second threshold is also obtained. The results contribute to building a comprehensive view of the magnetization manipulation by the spin Hall effect.

The paper is organized as follows. In Sec. II we provide a system description, and show the phase diagram of the magnetization in a steady state. In Sec. III the critical current formula destabilizing the magnetization from the initial state is derived. In Sec. IV the condition for a deterministic switching after turning off the current is studied. In Sec. V the comparison of the critical current with that in the different systems are discussed. Section VI summarizes the conclusion of this work.

II. SYSTEM DESCRIPTION

The system we consider is schematically shown in Fig. 1(a). The unit vector pointing in the magnetization
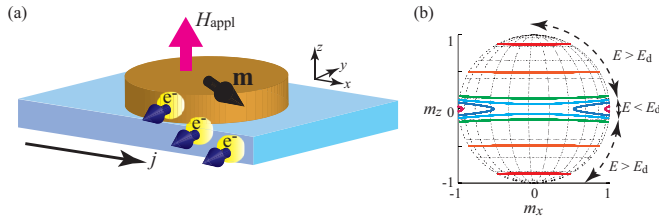
FIG. 1. (a) Schematic view of the system. The unit vector pointing in the magnetization direction is **m**. The electric current density and the external field are denoted as j and H_{appl}, respectively. (b) Schematic view of the constant energy curve in the absence of the external field.

direction of the ferromagnet is denoted as **m**. The z axis is perpendicular to the plane, while the x axis is parallel to the electric current density j in the nonmagnet. The spin Hall effect in the bottom nonmagnet generates pure spin-current flowing in the z direction with the spin polarization in the y direction, and excites the spin-transfer torque. An external field H_{appl} is applied in the z direction. The magnetization dynamics in the ferromagnet is described by the LLG equation,

$$\frac{d\mathbf{m}}{dt} = -\gamma\mathbf{m}\times\mathbf{H} - \gamma H_s\mathbf{m}\times(\mathbf{e}_y\times\mathbf{m}) + \alpha\mathbf{m}\times\frac{d\mathbf{m}}{dt}, \quad (1)$$

where γ and α are the gyromagnetic ratio and the Gilbert damping constant, respectively. The magnetic field is given by

$$\mathbf{H} = H_K m_x \mathbf{e}_x + (H_{appl} - 4\pi M m_z)\mathbf{e}_z, \quad (2)$$

where H_K is the in-plane magnetic anisotropy field in the x direction, whereas $-4\pi M$ is the shape anisotropy field in the z direction. The strength of the spin-transfer torque by the spin Hall effect is

$$H_s = \frac{\hbar\vartheta j}{2eMd}, \quad (3)$$

where ϑ is the spin Hall angle of the nonmagnetic heavy metal, and M and d are the saturation magnetization and thickness of the free layer, respectively. The values of the parameters used in this work are derived from typical experiments and simulations of the spin Hall phenomena and/or magnetic multilayers as $M = 1500$ emu/cm^3, $H_K = 200$ Oe, $\vartheta = 0.4$, $d = 1.0$ nm, $\gamma = 1.764\times10^7$ rad/(Oe s), and $\alpha = 0.005$ [13,31,32]; see also Appendix A for the calculation details.

We note that the macrospin model is used to derive the analytical formulas of the threshold currents. This model has been used to analyze the switching dynamics in both two-terminal and three-terminal devices [23,24,29,31–33]. It is known that the macrospin model is applicable to small devices. For example, the applicability of the model to the two-terminal perpendicularly magnetized system was investigated in Refs. [35–37]. The applicability of the macrospin model for the present three terminal was verified in the experiment carried out in Ref. [18], where the thickness of the free layer was 1.48 nm, whereas the short and long axes, corresponding to the y and x directions in the present geometry, were 160 and 400 nm, respectively. Therefore, we believe

that using the macrospin model is reasonable to analyze the switching behavior of the present system.

For the latter discussion, it is useful to introduce the magnetic energy density E as $E = -M\int d\mathbf{m}\cdot\mathbf{H}$,

$$E = -MH_{appl}m_z - \frac{MH_K}{2}m_x^2 + 2\pi M^2 m_z^2. \quad (4)$$

Note that the energy density E has two minima corresponding to

$$\mathbf{m}_{0\pm} = \begin{pmatrix}\pm m_{0x} \\ 0 \\ m_{0z}\end{pmatrix}, \quad (5)$$

where $m_{0z} = H_{appl}/(H_K + 4\pi M)$ and $m_{0x} = \sqrt{1-m_{0z}^2}$. The minimum energy density is

$$E_{min} = -M\frac{H_{appl}^2 + H_K(H_K + 4\pi M)}{2(H_K + 4\pi M)}. \quad (6)$$

The saddle point of the energy density locates at

$$\mathbf{m}_{d\pm} = \begin{pmatrix}0 \\ \pm m_{dy} \\ m_{dz}\end{pmatrix}, \quad (7)$$

where $m_{dz} = H_{appl}/(4\pi M)$ and $m_{dy} = \sqrt{1-m_{dz}^2}$. The saddle-point energy density is

$$E_d = -\frac{MH_{appl}^2}{8\pi M}. \quad (8)$$

An example of the constant energy line is shown in Fig. 1(b), where the external field is assumed to be zero; see also Appendix A for the values of the energy density. In this case ($H_{appl} = 0$) in particular, the minimum points locate at $\mathbf{m}_{0\pm} = \pm\mathbf{e}_x$, whereas the saddle points are $\mathbf{m}_{d\pm} = \pm\mathbf{e}_y$. These minimum and saddle points play a significant role in the determination of the switching condition, as discussed below.

Figure 2(a) summarizes m_x in a steady state in the presence of the current. The initial state is $\mathbf{m}_{0+}$, which is close to $m_x = 1$ shown by the red color. The magnetization stays near the initial state around small current and/or field regions. On the other hand, when the current magnitude becomes larger than critical values, the magnetization moves from the initial state. The critical current density is positive for $H_{appl} < 0$, whereas it becomes negative for $H_{appl} > 0$. In this paper we denote these critical current densities as $j_{c,+}$ and $j_{c,-}$, as shown in Fig. 2(a). Figure 2(b) shows m_x in a steady state, where the initial state is $\mathbf{m}_{0-}$ close to $m_x = -1$ shown by the blue color. Similar to Fig. 2(a), the magnetization moves from the initial state when the current density exceeds the critical value. In this case, the critical current is positive for $H_{appl} > 0$, whereas it becomes negative for $H_{appl} < 0$. The first purpose of the following discussion is to derive a theoretical formula of the critical currents to move the magnetization from the initial state.

It should also be noted that the magnetization state after turning off the current is also of interest, in particular for practical applications. Note that the magnetization finally saturates to $\mathbf{m}_{0+}$ or $\mathbf{m}_{0-}$ because these are energetically stable states.
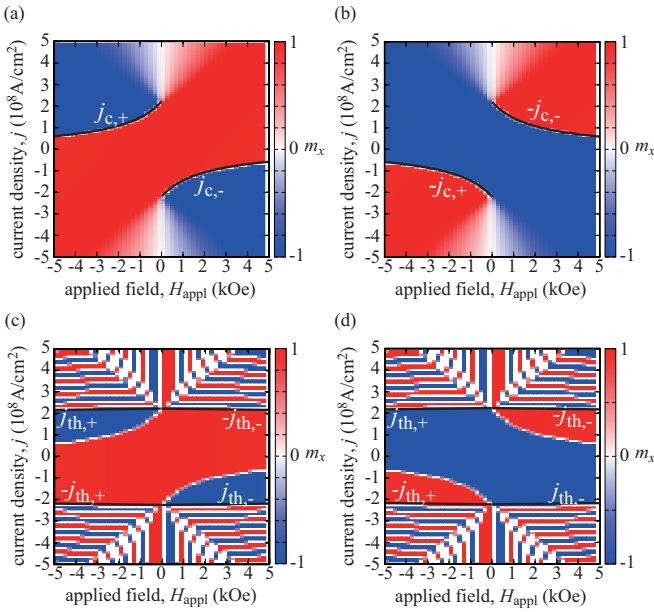
FIG. 2. Phase diagrams of m_x in a steady state (a) and (b) in the presence of the current, and (c) and (d) after turning off the current. The initial states are $\mathbf{m}_{0+}$ in (a) and (c), whereas it is $\mathbf{m}_{0-}$ in (b) and (d). The black lines with labels $\pm j_{c,\pm}$ and $\pm j_{th,\pm}$ in (a) and (b) and (c) and (d) correspond to Eqs. (17) and (20), respectively.

Figure 2(c) shows m_x in a steady state after the current is turned off, where the initial state is $\mathbf{m}_{0+}$. Comparing Fig. 2(c) with Fig. 2(a), the existence of another threshold current for the switching is found. For example, the relaxed state of the magnetization in Fig. 2(c) is $\mathbf{m}_{0-}$ ($m_x \simeq -1$ shown by the blue color) when the current density is slightly larger than the critical current density determining the boundary between the states of $m_x \simeq 1$ and $m_x \simeq -1$ found in Fig. 2(a). However, when the magnitude of the current density further increases, both $\mathbf{m}_{0+}$ (red) and $\mathbf{m}_{0-}$ (blue) states coexist, as can be seen in a large current region of Fig. 2(c). This fact indicates that, even if the magnetization direction moves to a position close to the switching state, which is $m_x \simeq -1$ in this case, by the spin-transfer torque, it moves back to the initial state ($m_x \simeq 1$), depending on the value of the current density. Therefore, the current density should be smaller than a certain value for a deterministic switching. In this paper we denote the threshold current density determining the upper boundary of the deterministic switching as $j_{th,\pm}$, as can be seen in Fig. 2(c). A similar behavior is observed when the initial state is $\mathbf{m}_{0-}$, as shown in Fig. 2(d). The second purpose of the following discussion is to clarify the origin of these complex phase diagrams and to derive the threshold current formula for the deterministic switching.

III. CRITICAL CURRENT FOR INSTABILITY THRESHOLD

In this section we derive the theoretical formula of the critical current density to move the magnetization from the initial state. First, we study the case of the zero-field switching. Second, the theory is extended to the case of the finite-field

switching. The role of the thermal fluctuation at finite temperature is also discussed.

A. Switching condition for zero-field case

Let us first investigate the magnetization dynamics in the absence of the external magnetic field. In the meantime we consider the dynamics caused by a positive current, and assume that the initial state is $\mathbf{m}_{0+}$, which is parallel to the x axis as $\mathbf{m}_{0+} = +\mathbf{e}_x$ for $H_{appl} = 0$.

We should first note the definition of the critical current density for the zero-field case. The spin-transfer torque due to the spin Hall effect moves the magnetization parallel to the y axis. The precession torque due to the magnetic field also becomes zero when the magnetization is parallel to the y axis because the point corresponds to the saddle point of the energy density. Therefore, the critical current density in the zero-field case is defined as a current density over which the magnetization saturates to the saddle point.

Figure 3(a) shows the time evolutions of the magnetization components, m_x (red), m_y (blue), and m_z (black), when the current density $j = 221 \times 10^6$ A/cm^2 is slightly smaller than the critical value. Although the magnetization moves from the initial state, it does not reach the saddle point. In particular, m_z moves from the initial state ($m_z = 0$) to a certain value monotonically.

On the other hand, Fig. 3(b) shows the dynamic trajectory of the magnetization when the current density $j = 222 \times 10^6$ A/cm^2 is larger than the critical value. Starting from the initial state $\mathbf{m}_{0+}$, the magnetization saturates to the saddle point $\mathbf{m}_{d-}$. Figure 3(c) shows the dynamic trajectory observed from a different view angle. The figure indicates that the magnetization first moves to the negative z direction, and then turns back to the xy plane because m_z is zero for both the initial ($\mathbf{m}_{0+}$) and final ($\mathbf{m}_{d-}$) states. This fact can also be confirmed from Figs. 3(d)–3(f), where the time evolutions of the magnetization components are shown. Whereas m_x and m_y shown in Figs. 3(d) and 3(e) monotonically moves from the initial to the final state, m_z in Fig. 3(f) shows a local minimum at which $dm_z/dt = 0$. The inset in Figs. 3(d)–3(f) indicate that the magnetization finally saturates to the saddle point $\mathbf{m}_{d-} = -\mathbf{e}_y$. Comparing Figs. 3(c)–3(f) with Fig. 3(a), we conclude that the existence of the point satisfying $dm_z/dt = 0$ determines a bifurcation between the switching and nonswitching states. Therefore, let us call the point of $dm_z/dt = 0$ as a critical point, for convention; see also Figs. 3(c) and 3(f), where the positions of the critical point in the real and time-domain spaces are shown, respectively.

Figure 3(b) also indicates that the switching occurs without accompanying magnetization precession. This is in contrast to the original idea of the spin-transfer torque switching [4,23,24], where the spin-transfer torque compensates for the damping torque, and therefore, the precession torque due to the magnetic field, corresponding to the first term on the right-hand side of Eq. (1), is dominant. The fact that the switching in the present system does not accompany precession dynamics implies that the switching occurs as a result of the competition between the precession torque and the spin-transfer torque. Therefore, the damping torque, which is proportional to the small constant α, can be neglected to
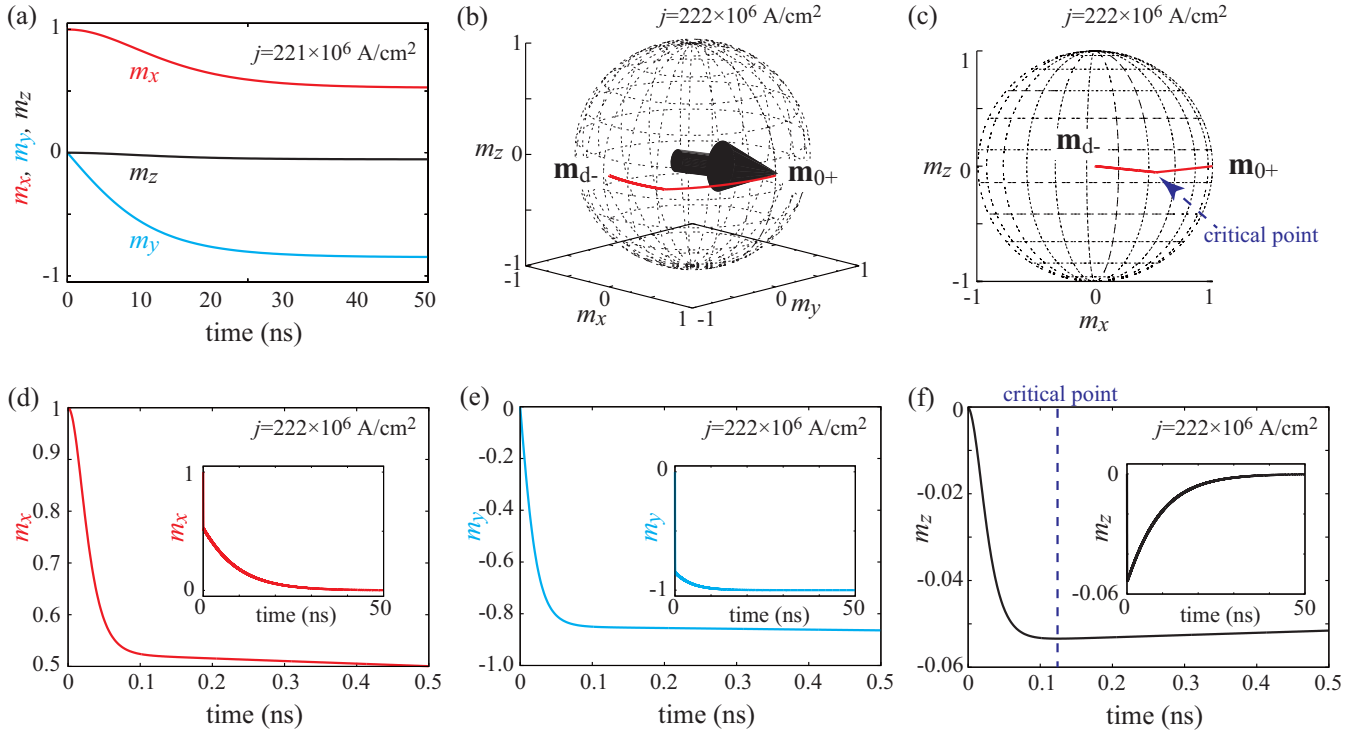
FIG. 3. (a) Time evolutions of the magnetization components for $j = 221 \times 10^6$ A/cm^2, which is slightly below the critical value. (b) and (c) Dynamic trajectories from different viewpoints, where the current density $j = 222 \times 10^6$ A/cm^2 is larger than the critical value. (d)–(f) Time evolutions of the magnetization components (red for m_x, blue for m_y, and black for m_z) for $j = 222 \times 10^6$ A/cm^2. The insets show the time evolutions in a long time range, indicating that the magnetization finally saturates to $\mathbf{m} = -\mathbf{e}_y$. The dotted arrow in (c) and line in (f) indicate the position satisfying $dm_z/dt = 0$, which is called a critical point. The external magnetic field is zero in these figures.

determine the switching condition. In fact, we confirmed from the numerical simulation that the critical current is unchanged even when we use a damping value of $\alpha = 0.02$, which is four times larger than that used in Fig. 3.

We note that the monotonic evolutions of m_x and m_y shown in Figs. 3(d) and 3(e) indicate that the signs of dm_x/dt and dm_y/dt are fixed. Therefore, the following conditions should be satisfied,

$$\frac{1}{\gamma} \frac{dm_x}{dt} \simeq (4\pi M m_z + H_s m_x) m_y < 0, \quad (9)$$

$$\frac{1}{\gamma} \frac{dm_y}{dt} \simeq -(H_K + 4\pi M) m_x m_z - H_s(m_x^2 + m_z^2) < 0, \quad (10)$$

Equations (9) and (10) should be satisfied for the switching process of $0 \leqslant m_x \lesssim 1$ and $-1 \lesssim m_y \leqslant 0$. Note that the critical point satisfying $dm_z/dt = 0$ exists when the switching occurs, as mentioned above. The LLG equation for m_z indicates that the critical point is determined by the condition

$$H_K m_x + H_s m_z = 0. \quad (11)$$

Substituting Eq. (11) into Eqs. (9) and (10), we find that the switching condition at the critical point becomes

$$\left(H_s - \frac{H_K 4\pi M}{H_s}\right) m_x > 0. \quad (12)$$

Since $m_x > 0$ during the switching in the present case, we find that Eq. (12) becomes $H_s > \sqrt{H_K 4\pi M}$, which gives the

critical current formulas as

$$j_c = \frac{2eMd}{\hbar \vartheta} \sqrt{H_K 4\pi M}. \quad (13)$$

The value of Eq. (13) for the present calculation is 221×10^6 A/cm^2, which shows good agreement with the numerical simulation shown in Fig. 3. Considering that the above discussion focuses on the switching by positive current, it should be mentioned that negative current can also induce the switching, where the critical current density is given by $-j_c$. We denote Eq. (13) as $j_{c,+}$, whereas $-j_c$ is denoted as $j_{c,-}$. When the initial state is $\mathbf{m}_{0-}$, $-j_{c,\pm}$ are the critical current densities.

We note that Eq. (13) can be derived from Eq. (12) without determining the value of m_x at the critical point. It is, however, useful to evaluate its value for the latter discussion. We find that m_x at the critical point is well approximated as (see also Appendix B)

$$m_x = \tfrac{1}{2}. \quad (14)$$

The numerically evaluated value of m_x at the critical point is 0.520 [see Fig. 3(d) and Appendix B], which is close to Eq. (14). In the next section we extend Eq. (14) to the finite field case to derive the critical current formula.

At the end of this section we would like to provide a brief comment on two timescales observed in Fig. 3. Whereas the magnetization moves from the initial state to the critical point fast, it takes a long time to saturate from the critical point to the fixed point ($\mathbf{m} \rightarrow -\mathbf{e}_y$). This result is in contrast with
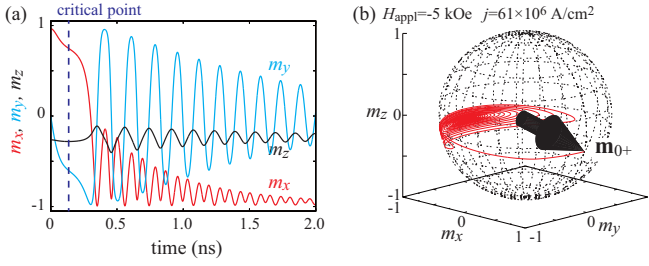
FIG. 4. (a) Time evolutions of the magnetization components and (b) its trajectory from $\mathbf{m}_{0+}$ for $j = 61 \times 10^6$ A/cm^2 and $H_{\mathrm{appl}} = -5$ kOe. The dotted line in (a) indicates the position of the critical point satisfying $dm_z/dt = 0$.

the spin-transfer torque switching in two-terminal devices, as well as that in the three-terminal type-Y device, where the switching time has a simple relation to the current as $1/t \propto j - j_c$ [23,38]. In addition, long-time dynamics as such are not observed for the switching in the presence of an external magnetic field, as shown in the next section. We note that investigating the origin of two timescales is of interest, and further work will be necessary in the future.

B. Switching condition for finite field case

Let us extend Eq. (13) to the system in the presence of a finite external field. Figures 4(a) and 4(b) show the time evolutions of the magnetization components and the dynamic trajectory for $j = 61 \times 10^6$ A/cm^2 and $H_{\mathrm{appl}} = -5.0$ kOe. The initial state is $\mathbf{m}_{0+}$. In comparison with the zero-field case shown in Fig. 3, the magnetization can move close to the switched state ($\mathbf{m}_{0-} \simeq -\mathbf{e}_x$). This is because the points at which the spin-transfer torque and the precession torque

due to the magnetic field become zero are different from the case without external magnetic field. We also notice that the magnetization does not show a precessional motion before ($t \lesssim 0.3$ ns) reaching the boundary ($m_x = 0$) between two stable states, although the precessional motion appears after the magnetization overcomes the boundary. This fact indicates that the critical current is mainly determined by the competition between the precession and spin-transfer torques, as in the case of the zero-field switching. In fact, we confirm that the critical current density is 63×10^6 A/cm^2 for $\alpha = 0.02$, which is close to that for $\alpha = 0.005$, indicating that the damping torque does not play a critical role to determine the instability threshold. The fact that the switching occurs without accompanying the precessional motion also indicates that the conditions that dm_x/dt and dm_y/dt have fixed signs, used in the derivation of Eq. (13), can also be used for the derivation of the critical current formula. Then, we find that the critical current density can be determined by the following condition:

$$-H_{\mathrm{appl}} + \left(H_{\mathrm{s}} - \frac{H_{\mathrm{K}} 4\pi M}{H_{\mathrm{s}}} \right) m_x > 0. \qquad (15)$$

Equation (15) becomes Eq. (12) in the limit of $H_{\mathrm{appl}} \to 0$. We should, however, evaluate the value of m_x at the critical point for the finite field case, in contrast with the derivation of Eq. (13) where evaluating the value of m_x in Eq. (12) was not necessary. For example, the critical point satisfying $dm_z/dt = 0$ appears at $t = 0.133$ ns for $j = 61 \times 10^6$ A/cm^2 and $H_{\mathrm{appl}} = -5.0$ kOe, as shown by the dotted line in Fig. 4(a). To proceed with the analysis, we extend the derivation of Eq. (14) to the finite field case, and find that m_x at the critical point is given by (see also Appendix B)

$$m_x = \frac{H_{\mathrm{K}}(H_{\mathrm{K}} + 4\pi M)H_{\mathrm{s}}}{2H_{\mathrm{K}}H_{\mathrm{s}}\sqrt{(H_{\mathrm{K}} + 4\pi M + H_{\mathrm{appl}})(H_{\mathrm{K}} + 4\pi M - H_{\mathrm{appl}})} + H_{\mathrm{appl}}\left(H_{\mathrm{s}}^2 - H_{\mathrm{K}}^2\right)}. \qquad (16)$$

For example, the value of Eq. (16) for $j = 61 \times 10^6$ A/cm^2 and $H_{\mathrm{appl}} = -5.0$ kOe is 0.755, which is close to the result of the numerical simulation in Fig. 3(a), where $m_x = 0.750$ at the critical point appeared. Substituting Eq. (16) into Eq. (15), we find that the critical current density for the finite field case is given by

$$j_{\mathrm{c},\pm} = \pm \frac{2eMd}{\hbar\vartheta} \frac{H_{\mathrm{K}}(H_{\mathrm{K}} + 4\pi M)\sqrt{H_{\mathrm{K}} 4\pi M} \pm H_{\mathrm{appl}}H_{\mathrm{K}}\sqrt{(H_{\mathrm{K}} + 4\pi M + H_{\mathrm{appl}})(H_{\mathrm{K}} + 4\pi M - H_{\mathrm{appl}})}}{H_{\mathrm{K}}(H_{\mathrm{K}} + 4\pi M) - H_{\mathrm{appl}}^2}. \qquad (17)$$

Note that $j_{\mathrm{c},+}$ is the critical current density for $H_{\mathrm{appl}} > 0$, whereas $j_{\mathrm{c},-}$ is that for $H_{\mathrm{appl}} < 0$. On the other hand, when the initial state is $\mathbf{m}_{0-}$, the critical current density for $H_{\mathrm{appl}} > (<)0$ is $-j_{\mathrm{c},-(+)}$. The value of $j_{\mathrm{c},+}$ estimated from Eq. (17) is 59×10^6 A/cm^2 for $H_{\mathrm{appl}} = -5.0$ kOe, which shows good agreement with the result of the numerical simulation where the switching occurs for the current density of $j = 61 \times 10^6$ A/cm^2, as shown in Fig. 4(a).

C. Dynamics at finite temperature

This work mainly focuses on the magnetization dynamics at zero temperature to derive the critical current formula for the switching. Simultaneously, however, the role of the

thermal fluctuation at finite temperature [39] is also of great interest. In this section we discuss the magnetization dynamics at finite temperature by solving the LLG equation with the random torque numerically. In particular, we focus on the current range near the critical value j_c where the thermal fluctuation is expected to play a critical role on the magnetization switching [29,38,40–52].

The thermal fluctuation provides a torque,

$$\boldsymbol{\tau} = -\gamma \mathbf{m} \times \mathbf{h}, \qquad (18)$$

which should be added to the right-hand side of Eq. (1). The components $h_k(t)$ ($i = x, y, z$) of the random field $\mathbf{h}$ obeys the
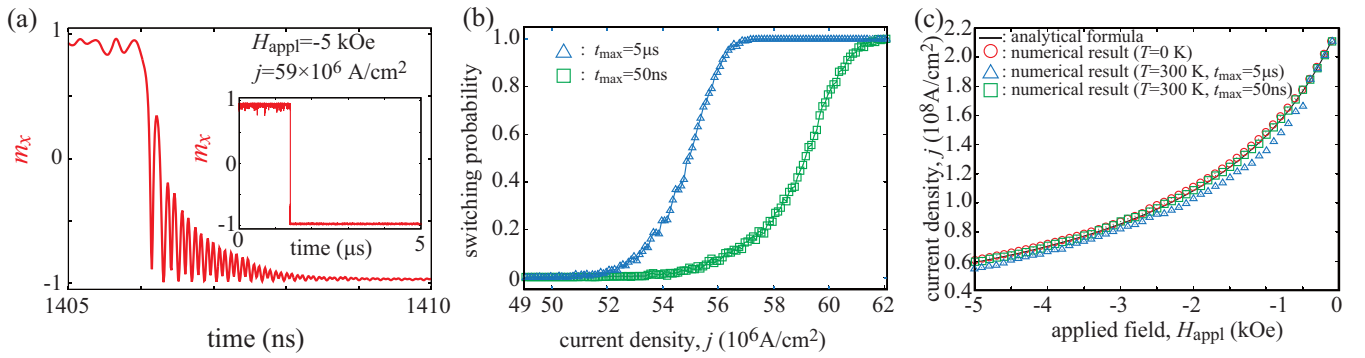
FIG. 5. (a) An example of the magnetization dynamics at finite temperature, where $H_{\rm appl} = -5.0$ kOe and $j = 59 \times 10^6$ A/cm^2. The main figure shows the time evolution of m_x near the switching, whereas the inset shows that over a long range of time. (b) Dependencies of the switching probabilities $P(j)$ on the current density for the current pulses of 5 μs (blue triangles) and 50 ns (green squares). The switching probability is evaluated from the 1000 trials of the LLG equation, where the initial state is reset at every trial. (c) The dependencies of the current density maximizing $dP(j)/dj$ on the external magnetic field for the long (blue triangles) and short (green squares) pulses. For comparison, the critical current densities at zero temperature, estimated from Eq. (17) (black line), and the numerical simulation (red circles) in Sec. III B are also shown.

fluctuation-dissipation theorem [39],

$$\langle h_k(t) h_\ell(t') \rangle = \frac{2\alpha k_{\rm B} T}{\gamma M V} \delta_{k\ell} \delta(t - t'), \qquad (19)$$

where $V = Sd$ is the volume of the free layer consisting of the cross-section area S and the thickness d. According to Ref. [18] where the applicability of the macrospin model was confirmed, we assume that $S = \pi \times 80 \times 200$ nm^2. The temperature T is fixed to $T = 300$ K. The calculation method to solve Eq. (1) with Eq. (18) are summarized in Appendix C.

Figure 5(a) shows an example of the magnetization dynamics at finite temperature, where the external magnetic field and the current density are $H_{\rm appl} = -5.0$ kOe and $j = 59 \times 10^6$ A/cm^2, respectively. We remind the readers that the critical current density estimated from the numerical simulation at zero temperature is 61×10^6 A/cm^2, as mentioned in Sec. III B. The figure is an enlarged view near the switching, whereas the inset shows the time evolution of m_x over a long range of time ($0 \leqslant t \leqslant 5$ μs). Since the current density is smaller than the critical value at zero temperature, the magnetization stays near the initial state with random motion for a long time. When, however, the magnetization comes close to the critical point and the random torque further assists the motion to overcome the point, the switching is achieved.

Next, let us show the dependence of the switching probability P on the current density. We note that the existence of the random torque does not guarantee the switching, although Fig. 5(a) shows an example of the probabilistic switching. We also emphasize that the time at which the switching occurs is random. In particular, we note that a long time is necessary to observe a finite probabilistic switching, especially for the current density much lower than the critical value at zero temperature. On the other hand, for practical purpose, a short current pulse is used to achieve a fast switching. Therefore, we calculate the switching probabilities for both long ($t_{\rm max} = 5$ μs) and short ($t_{\rm max} = 50$ ns) current pulses, where we regard the magnetization switched when, starting from the initial condition $m_x(t = 0) > 0$, the magnetization at $t = t_{\rm max}$ satisfies $m_x(t = t_{\rm max}) < 0$; see also Appendix C

for the evaluation method of the switching probability. Figure 5(b) shows the switching probabilities for the cases of the long (blue triangles) and short (green squares) pulses, where $H_{\rm appl} = -5.0$ kOe. For the case of the long pulse, the switching is observed even at the current density relatively smaller than the critical value (61×10^6 A/cm^2) evaluated by the LLG simulation at zero temperature. The switching probability shows a gradual evolution from $P = 0$ to $P = 1$. On the other hand, the switching probability increases near the critical current density for the short-pulse case. Figure 5(c) summarizes the magnetic field dependence of the current density at which the switching probability increases most rapidly, i.e., the current density maximizing $dP(j)/dj$, which is regarded as the switching current density at finite temperature. For comparison we also shows the critical current density at zero temperature, where the black line is obtained from Eq. (17), whereas the red circles are obtained by the numerical simulation, as done in Sec. III B. For the long-pulse ($t_{\rm max} = 5$ μs) case, the switching current densities at finite temperature are reduced to roughly 90% of those at zero temperature; for example, the switching current density for $H_{\rm appl} = -5.0$ kOe is estimated to be 54.8×10^6 A/cm^2, whereas that for zero-temperature case was 61×10^6 A/cm^2, as mentioned in Sec. III B. On the other hand, the switching current densities for the short-pulse ($t_{\rm max} = 50$ ns) case are slightly lower but nearly overlap the zero-temperature results; for example, the switching current for $H_{\rm appl} = -5.0$ kOe is estimated to be 59.7×10^6 A/cm^2. These results indicate that, although the thermal fluctuation provides a possibility to switching the magnetization by the current lower than the critical value, the critical current formulas derived in this work will be useful to analyze the magnetization switching, particularly for a short-pulse switching required in practical applications.

D. Summary of this section

In this section we derive the critical current formula to move the magnetization from the initial state. The main results are Eqs. (13) and (17). Equation (13) is the critical current

formula for the zero-field case, whereas Eq. (17) is the extension to the finite field case. Equation (17) reproduces Eq. (13) in the limit of $H_{\text{appl}} \to 0$.

The black solid lines in Figs. 2(a) and 2(b) are $j_{c,\pm}$ and $-j_{c,\pm}$ respectively. As shown, the formula of the critical current density given by Eq. (17) well explains the boundary between the initial and switching states in the presence of the current, showing the validity of Eq. (17).

IV. DETERMINISTIC SWITCHING

Finally, we discuss the theoretical condition for the deterministic switching. In many cases including practical purposes, the magnetization state not only in the presence of the current but also the state after turning off the current is of great interest. The phase diagrams in Figs. 2(c) and 2(d) reveal the existence of the current range in which a deterministic switching is achieved, as mentioned in Sec. II. For example, for $H_{\text{appl}} = -5.0$ kOe, the deterministic switching occurs in the current range of $70 \leqslant j \leqslant 270 \times 10^6$ A/cm^2, as shown in Fig. 2(c), where the lower boundary, 70×10^6 A/cm^2 is well explained by Eq. (17). Here we note that the current density in Fig. 2 varies by 10×10^6 A/cm^2 step, and thus, the deterministic switching range here is mentioned as $70 \leqslant j \leqslant 270 \times 10^6$ A/cm^2. However, to be more precise, as mentioned in Sec. III, the detail value of the lower boundary is 61×10^6 A/cm^2. There is, in addition, another threshold value, which is 270×10^6 A/cm^2 in this example. Above this second threshold, both $\mathbf{m}_{0+}$ (red) and $\mathbf{m}_{0-}$ (blue) appear as a final state, as shown in Fig. 2(c), which is sensitive to the values of the parameters such as the current and field. Let us derive the theoretical formula of the second threshold current here.

Before the discussion we briefly note that the word "deterministic" in this section is used to express the switching which is not sensitive to the values of the external magnetic field and the current density, and is not used to distinguish from the dynamics at finite temperature studied in Sec. III C. Since the phase diagram in Fig. 2 is obtained by the zero-temperature simulation, the magnetization states are determined deterministically. The results in Fig. 2 reveal, however, that there are the regions where the relaxed state of the magnetization is sensitive to the values of the external magnetic field and the current density, even at zero temperature. Such a region should be avoided for practical purposes because careful control of the field and/or current is required for reliable operations.

Note that the switched and nonswitched states coexist above this second threshold, and as a result, the phase diagram shows a complex structure, as shown in Figs. 2(c) and 2(d). We notice that such a complex structure appears due to the magnetization precession around the hard (z) axis. To explain this behavior we show the constant energy curve of the ferromagnet in the presence of the external field in Fig. 6(a); see also Appendix A. There are two energetically stable states bounded by $\mathbf{m}_{0\pm}$ and $\mathbf{m}_{d\pm}$. The stable states correspond to the region of $E < E_d$ in Fig. 6(a), where the saddle-point energy density is given by Eq. (8). There are also two energetically unstable states, corresponding to the region of $E > E_d$. After turning off the current, the magnetization starts the precession on the constant energy curves, and slowly relaxes to the stable
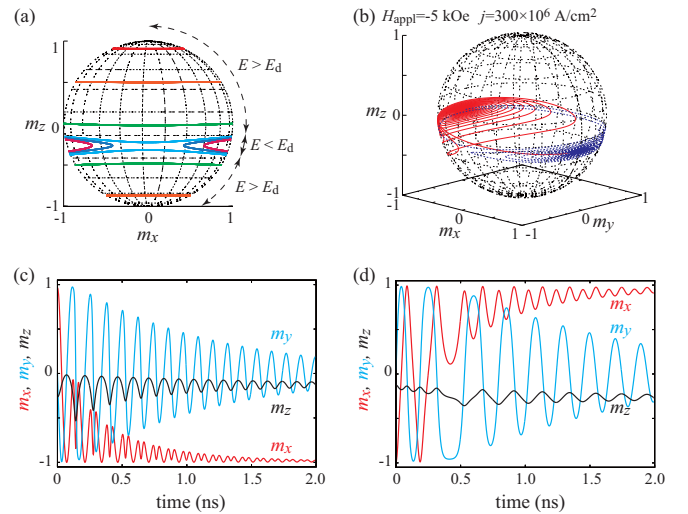

FIG. 6. (a) Schematic view of the constant energy lines for $H_{\text{appl}} = -5.0$ kOe. (b) The red solid line is the trajectory of the magnetization for $j = 300 \times 10^6$ A/cm^2 and $H_{\text{appl}} = -5$ kOe. The blue dotted line represents the trajectory after turning off the current. Time evolutions of the magnetization components in the presence of the current and after turning off the current are shown in (c) and (d), where the origin of the time is set to be $t = 0$ in (d), for simplicity. Practically, the dynamics starts after turning off the current.

states. The magnetization directly relaxes to the closest stable state when the steady-state solution in the presence of the current locates inside one of the stable regions, i.e., when the energy density given by Eq. (4) with $\mathbf{m}$ in the presence of the current is smaller than E_d. In this case, the deterministic switching can be realized. On the other hand, when the steady-state solution in the presence of the current locates in one of the unstable states, the magnetization first starts the precession on the constant energy curves around the z axis. In this case, even if the magnetization in the presence of the current is close to the switched state, the magnetization can switch back near the initial state. Figure 6(b) shows an example of such a dynamics, where the red solid line represents the dynamic trajectory in the presence of the current, whereas the blue dotted line shows the relaxation dynamics after turning off the current. Figures 6(c) and 6(d) show the time evolutions of the magnetization components in the presence of the current and after turning off the current, respectively. Although the magnetization moves close to the switched state ($\mathbf{m} \simeq -\mathbf{e}_x$) when the current is injected, it turns back close to the initial state ($\mathbf{m} \simeq +\mathbf{e}_x$) due to the precession around the hard (z) axis. Such a dynamics is the origin of the complex structure in the phase diagram in Fig. 2(c).

Summarizing these considerations, the second threshold current bounding the deterministic switching to $\mathbf{m}_{0-}$ is derived from the condition that the steady-state solution locates inside the energetically stable region, and is given by (see also Appendix D)

$$j_{\text{th},\pm} = \frac{2eMd}{\hbar\vartheta} \frac{H_{\text{appl}}H_K \pm \sqrt{H_K 4\pi M (H_K + 4\pi M)}}{4\pi M}. \quad (20)$$

We note that $j_{\text{th},+(-)}$ for a negative (positive) H_{appl} is the threshold current density to guarantee that the final state after

turning off the current is $\mathbf{m}_{0-}$, whereas $-j_{\text{th},\pm}$ for a negative (positive) field determines the boundary that the final state is $\mathbf{m}_{0+}$. The black solid lines in Figs. 2(c) and 2(d) are Eq. (20) and $-j_{\text{th},\pm}$ for these cases, indicating the validity of the formula.

In summary, the existence of the threshold current below which the deterministic switching is achieved is found. We remind the readers that the critical current formula derived in Sec. III determines the instability threshold to move the magnetization from the initial state. On the other hand, the threshold current formula derived in this section determines the relaxed state of the magnetization after turning off the current. Summarizing these discussions, the current density j should be in the range determined by two current scales. For example, the current density should be in the range of $j_{\text{c},+} < j < j_{\text{th},+}$ for the deterministic switching when the external field is applied to the negative z direction ($H_{\text{appl}} < 0$) and the initial state is close to the positive x direction ($\mathbf{m}_{0+}$), as shown in Fig. 2(c).

V. COMPARISON TO OTHER SYSTEMS

In this section we discuss the comparison between the present and previous works.

First, we mention that the experimentally observed value of the critical current density for the same device structure in Ref. [18] is, at maximum, one order of magnitude smaller than that found in the present work in the small H_{appl} limit. This is because both the in-plane and perpendicular magnetic anisotropy fields are one order of magnitude smaller than those used in the present work. As implied from Eq. (13), the critical current density of the present system is roughly scaled as $\sqrt{H_{\text{K}} 4\pi M}$ in the small H_{appl} limit. Therefore, the critical current density in Ref. [18] was small due to the smallness of H_{K} and $4\pi M$. In Ref. [18] the perpendicular demagnetization field $4\pi M$ is suppressed by using the interfacial magnetic anisotropy effect at the CoFeB/MgO interface [53–55].

When we compare the the critical current of the present system, named as type X, with another system named type Y, we should first emphasize that a fair comparison is difficult because the deterministic switching in the type-X device requires the external magnetic field, whereas the switching in the type-Y device can be achieved without, in principle, applying the external field. The experimentally observed value of the critical current density for the type-Y device was on the order of 10^7 A/cm^2 [8], which was well explained by the critical current formula derived by the macrospin assumption. The critical current density of the type-X system can be either small or large compared with this value, depending on the magnitude of the applied field. If we focus on the small field limit, however, the type Y shows a small critical current density compared with that in the type X. This is due to the smallness of the damping constant. The critical current density of the type-Y device is proportional to the damping constant α [23,24], whereas the dependence of the critical current density of the type-X device on the damping constant is weak, as mentioned above. The ratio of these two critical current densities are roughly given by $j_{\text{c}}^{\text{type Y}}/j_{\text{c}}^{\text{type X}} \sim \alpha\sqrt{4\pi M/H_{\text{K}}}$, where we use Eq. (13) and the fact that the critical current density in the type-Y device is

given by $j_{\text{c}}^{\text{type Y}} \simeq [2\alpha e M d/(\hbar\vartheta)](H_{\text{K}} + 2\pi M)$. The damping constant of the ferromagnet, such as CoFeB, conventionally used in spintronics devices is on the order of 10^{-3}–10^{-2} [56]. Therefore, the critical current density of the type-Y device is usually smaller than that of the type-X device, even though $4\pi M/H_{\text{K}} \gg 1$. Regarding these facts, the type-Y device has several advantages, such as the zero-field switching and small critical current, with respect to the type-X device. However, we emphasize that the fast switching in the type-X device is preferable for practical applications, compared with a slow switching in the type-Y devices.

The critical current density of the type-Z device has been found to be on the order of 10^6–10^8 A/cm^2 [7,10–17,26,27], which are comparable to that found in the type-X device. In both the type-X and type-Z devices, the external magnetic field is necessary for the deterministic switching. We note that the critical current densities of both type X and type Z are nearly independent of the damping constant [28,32], and are dominated by the perpendicular magnetic anisotropy field. We should, however, note that the roles of the perpendicular magnetic anisotropy field on these devices are different. The perpendicular magnetic anisotropy field in the type-Z device has a positive sign, indicating the magnetic easy axis is parallel to the z axis. The perpendicular magnetic anisotropy energy of the type-Z device determines the thermal stability of the ferromagnet. On the other hand, the perpendicular magnetic anisotropy field in the type-X device, $-4\pi M$, has a negative sign, indicating that the in-plane magnetized state is energetically stable. The thermal stability of the ferromagnet is determined by the in-plane magnetic anisotropy field H_{K}. Therefore, the low critical current density and sufficient thermal stability might be simultaneously achieved in the type-X device by suppressing the perpendicular magnetic anisotropy field by, for example, the interfacial effect [53–55]. It should, however, be noted that the current-field range for the deterministic switching, bounded by j_{c} and j_{th} in Fig. 2, is relatively narrow in the type-X device compared with that of the type-Z device; see Ref. [32], where we note that the spin Hall angle used in the calculations in Ref. [32] is smaller than that in the present work. This result means that the type-Z device has wide tunability of the external parameters (current and field) compared with the type-X device.

Summarizing these switching properties, the three device structures, type X, Y, and Z, have both advantages and disadvantages for practical applications. An appropriate choice of the device structure, depending on the purpose, will be necessary.

VI. CONCLUSION

In conclusion, theory of the magnetization switching caused by the spin Hall effect was developed for a ferromagnet having the easy axis parallel to the current direction. The analytical formula of the critical current for the magnetization switching was obtained from the theoretical condition of monotonic switching as a result of the competition between the spin-transfer torque and the precession torque. It was also found that a deterministic magnetization switching after turning off the current is achieved only when the current is in a certain range determined by another threshold current.

Outside the current range, the final state of the magnetization becomes sensitive to the parameters such as the current and the magnetic field, and therefore, a precise manipulation of the magnetization becomes difficult. This is because the spin-transfer torque due to a large current brings the magnetization in an energetically unstable state, and induces the magnetization precession around the hard axis. The theoretical formula of another threshold current was also derived, showing good agreement with the result of numerical simulation. Summarizing these results, the current density for the deterministic switching should be in a certain range determined by two current scales. These results provide a solid direction for designing the three-terminal magnetic devices with in-plane easy axis.

ACKNOWLEDGMENTS

APPENDIX A: CALCULATION DETAILS AT ZERO TEMPERATURE

The LLG equation was solved by the fourth-order Runge-Kutta method with the time step of 5×10^{-3} ns. First, we solve the LLG equation with the current (spin-transfer torque) from $t = 0$ to $t = 5$ μs, and estimate the fixed point the magnetization saturates. In general, the time range ($t_{\max} = 5$ μs) is sufficient to evaluate the saturated state of the magnetization. After that, second, we solve the LLG equation without the current to evaluate the relaxed state of the magnetization. In the first step, the initial state of the magnetization is chosen to be the energetically minimum point, whereas the initial state of the second step is the fixed point obtained by the first step.

The constant energy curves in Figs. 1(b) and 6(a) are obtained by solving the Landau-Lifshitz (LL) equation, where the damping constant α and the current density j are set to be zero. In Fig. 1(b), the constant energy curves, from top to bottom, are obtained by the LL equation with the initial conditions of $\theta = 30°$ (top red), $60°$ (top orange), $80°$ (top green), $83°$ (top light blue), $85°$ (purple), $88°$ (red-purple), $97°$ (bottom light blue), $100°$ (bottom green), $120°$ (bottom orange), and $150°$ (bottom red) with $\varphi = 0°$ or $180°$, where the zenith and azimuth angles θ and φ are defined as $\mathbf{m} = (\sin\theta\cos\varphi, \sin\theta\sin\varphi, \cos\theta)$. The corresponding energy densities estimated from Eq. (4) are 10.54, 3.42, 0.28, 0.06, -0.04, -0.13×10^6 erg/cm³ for $\theta = 30°, 60°, 80°, 83°,$ $85°$, and $88°$, respectively. Note that the energy density is the same for θ and $180° - \theta$ in Fig. 1(a) because the external field is absent. On the other hand, Fig. 6(a) is obtained by solving the LL equation with the initial conditions of $\theta = 30°$ (top red), $60°$ (top orange), $90°$ (top green), $99°$ (top light blue), $100°$ (purple), $101°$ (red-purple), $112°$ (bottom light blue), $120°$ (bottom green), and $150°$ (bottom orange), corresponding to the energy densities of 17.06, 7.17, -0.15, -0.97, -1.02, -1.06, -0.95, -0.33, and 4.07×10^6 erg/cm³. We should emphasize here that Figs. 1(b) and 6(a) are made to
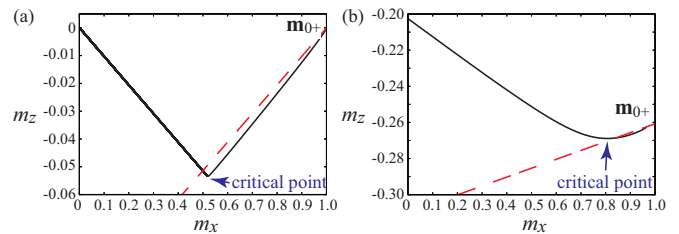

FIG. 7. The dynamic trajectories of the magnetization in the xz plane obtained from the numerical simulation of Eq. (1) (black solid lines) and the approximated trajectories near the initial state estimated from Eqs. (B2) and (B4) (red dashed lines). The values of the external magnetic field H_{appl} and the current density j are (a) 0 Oe and 222×10^6 A/cm², and (b) -5.0 kOe and 70×10^6 A/cm², respectively. The position of the initial state is indicated as $\mathbf{m}_{0+}$, whereas the location of the critical point satisfying $dm_z/dt = 0$ is indicated by the blue arrow.

catch the overviews of the energy landscapes, and these values of the energy density are not explicitly used to develop the theory in the main text.

APPENDIX B: DYNAMIC TRAJECTORY FROM THE INITIAL STATE

In this Appendix we discuss the derivations of Eqs. (14) and (16). The initial state is $\mathbf{m}_{0+}$, for convention.

First, let us consider the zero-field case. We notice that the dynamic trajectory from the initial state to the critical point in the xz plane is well approximated to be linear, as can be seen in Fig. 3(c). The gradient of this approximated linear line is given by

$$\frac{\dot{m}_z}{\dot{m}_x} = \frac{H_K m_x + H_s m_z}{4\pi M m_z + H_s m_x}, \quad (B1)$$

where the damping torque is neglected, as mentioned in the main text. Substituting $\mathbf{m}_{0+} = (1, 0, 0)$ for $H_{\text{appl}} = 0$ into Eq. (B1), the dynamic trajectory in the xz plane with a linear approximation is described as

$$m_z = \frac{H_K}{H_s}(m_x - 1). \quad (B2)$$

Figure 7(a) shows the dynamic trajectory of the magnetization in the xz plane obtained from the numerical simulation of Eq. (1) by the black solid line, whereas the red dashed line is Eq. (B2). The values of the parameters are $H_{\text{appl}} = 0$ and $j = 222 \times 10^6$ A/cm², as in the case of Fig. 3(c). As shown, approximation obtained as Eq. (B2) well describes the dynamic trajectory from the initial state $\mathbf{m}_{0+}$ to the critical point. The intersection between Eq. (11) and (B2) is the critical point at zero field, which is given by Eq. (14). As mentioned in the main text, the numerically evaluated value of m_x at the critical point satisfying $dm_z/dt = 0$ is 0.520, which is close to Eq. (14).

Next, let us extend the above discussion to the finite field case. We again approximate the dynamic trajectory from the initial state to the critical point to be linear. The gradient of

the linear line is

$$\frac{\dot{m}_z}{\dot{m}_x} = \frac{H_\text{K} m_x + H_\text{s} m_z}{-H_\text{appl} + 4\pi M m_z + H_\text{s} m_x}. \quad \text{(B3)}$$

Therefore, the approximated dynamic trajectory in the xz plane is

$$m_z = \frac{H_\text{K} m_{0x} + H_\text{s} m_{0z}}{-H_\text{appl} + 4\pi M m_{0z} + H_\text{s} m_{0x}} (m_x - m_{0x}) + m_{0z}, \quad \text{(B4)}$$

where m_{0x} and m_{0z} are given by Eq. (5). Figure 7(b) shows the dynamic trajectory of the magnetization in the xz plane obtained from the numerical simulation of Eq. (1) by the black solid line, whereas the red dashed line is Eq. (B4). The values of the parameters are $H_\text{appl} = -5.0$ kOe and $j = 70 \times 10^6$ A/cm^2, as in the case of Fig. 4(b). Again, using Eq. (B4) as an approximation well describes the dynamic trajectory from the initial state $\mathbf{m}_{0+}$ to the critical point. The numerically evaluated value of m_x at the critical point satisfying $dm_z/dt = 0$ is 0.806, which is close to the value of 0.828 estimated as the intersection between Eq. (11) and (B4), as mentioned in the main text.

APPENDIX C: CALCULATION METHOD AT FINITE TEMPERATURE

The LLG equation, with the random torque given by Eq. (18), is solved by adding the random field satisfying Eq. (19) to the magnetic field $\mathbf{H}$ in Eq. (1) [57]. The k component ($k = x, y, z$) of the random field is given by

$$h_k(t) = \sqrt{\frac{2\alpha k_\text{B} T}{\gamma M V \Delta t}} \xi_k(t), \quad \text{(C1)}$$

where the time step of the numerical simulation is $\Delta t = 5 \times 10^{-3}$ ns, as mentioned in Appendix A. White noise ξ is derived from two random numbers, ζ_k and ζ_ℓ, in the range of $0 < \zeta_k, \zeta_\ell \leqslant 1$ by the Box-Muller transformation as $\xi_k = \sqrt{-2 \log \zeta_k} \sin(2\pi \zeta_\ell)$ and $\xi_\ell = \sqrt{-2 \log \zeta_k} \cos(2\pi \zeta_\ell)$.

We calculate the LLG equation with the white noise $N = 1000$ times for a given set of the applied field H_appl and the current density j to evaluate the switching probability. Starting from the initial state in the positive x region, we evaluate the x component m_x of the magnetization at $t_\text{max} = 5$ μs or $t = 50$ ns. We note that the time step Δt is kept to 5×10^{-3} ns for both cases. We count the number n of the trial where $m_x(t_\text{max}) < 0$, and define the switching probability as $P(j) = n/N$. We note that the initial state is reset at each trial. The range of the current density for the switching probability is chosen as $j_{c,+} - \Delta j_1 \leqslant j \leqslant j_{c,+} + \Delta j_2$ with the step of $\delta j = 0.1 \times 10^6$ A/cm^2, where $j_{c,+}$ is the analytical value of the critical current density given by Eq. (17),

whereas $\Delta j_1 = 10 \times 10^6$ A/cm^2 and $\Delta j_2 = 3 \times 10^6$ A/cm^2. The probability density is calculated as $dP(j)/dj \propto [P(j + \delta j) - P(j - \delta j)]/2$ to evaluate the current density where the switching probability increases most rapidly.

APPENDIX D: BOUNDARY OF DETERMINISTIC SWITCHING

In this Appendix we show the derivation of Eq. (20). As mentioned in the main text, the deterministic switching occurs when the steady-state solution in the presence of the current locates inside one of the energetically stable regions. The result of the numerical simulation indicates that the steady-state solution in the presence of finite field and current locates at $m_y = 0$; see, for example, Figs. 4(a) and 4(b). We notice that $dm_x/dt = 0$ and $dm_z/dt = 0$ are naturally satisfied at this point, as can be confirmed from the LLG equations for m_x and m_z. On the other hand, using $m_y = 0$, the condition of the steady state for m_y, $dm_y/dt = 0$, becomes

$$-H_\text{appl} m_x + (H_\text{K} + 4\pi M) m_x m_z = -H_\text{s}. \quad \text{(D1)}$$

Although an exact solution satisfying Eq. (D1) can be obtained by, for example, introducing a variable θ defined as $m_x = \sin\theta$ and $m_z = \cos\theta$, the solution is complex and is not useful. Instead, we use the fact that the switched state $\mathbf{m}_{0-}$ is close to the easy axis direction $-\mathbf{e}_x$. Then, $m_x \simeq -1$ and $m_z \simeq (H_\text{appl} + H_\text{s})/(H_\text{K} + 4\pi M)$. Substituting these values into Eq. (4), we find that the energy density at the steady state is approximately given by

$$E_- = -MH_\text{appl} \left(\frac{H_\text{appl} + H_\text{s}}{H_\text{K} + 4\pi M} \right) - \frac{MH_\text{K}}{2}$$
$$+ 2\pi M^2 \left(\frac{H_\text{appl} + H_\text{s}}{H_\text{K} + 4\pi M} \right)^2. \quad \text{(D2)}$$

On the other hand, the saddle-point energy density is given by Eq. (8). The condition that $E_- < E_\text{d}$ gives Eq. (20), which is the threshold current density for the deterministic switching to the stable state of $\mathbf{m}_{0-}$.

We note that the condition to keep the magnetization near the initial state can also be derived in a similar way. In this case, $m_x \simeq +1$ and $m_z = (H_\text{appl} - H_\text{s})/(H_\text{K} + 4\pi M)$. The energy density at this point is

$$E_+ = -MH_\text{appl} \left(\frac{H_\text{appl} - H_\text{s}}{H_\text{K} + 4\pi M} \right) - \frac{MH_\text{K}}{2}$$
$$+ 2\pi M^2 \left(\frac{H_\text{appl} - H_\text{s}}{H_\text{K} + 4\pi M} \right)^2. \quad \text{(D3)}$$

The threshold current for the switching to $\mathbf{m}_{0+}$ obtained from the condition $E_+ < E_\text{d}$ is $-j_{\text{th},\pm}$.

[1] M. I. Dyakonov and V. I. Perel, Current-induced spin orientation of electrons in semiconductors, Phys. Lett. A **35**, 459 (1971).

[2] J. E. Hirsch, Spin Hall Effect, Phys. Rev. Lett. **83**, 1834 (1999).

[3] Y. K. Kato, R. C. Myers, A. C. Gossard, and D. D. Awschalom, Observation of the spin Hall effect in semiconductors, Science **306**, 1910 (2004).

[4] J. C. Slonczewski, Current-driven excitation of magnetic multilayers, J. Magn. Magn. Mater. **159**, L1 (1996).

[5] L. Berger, Emission of spin waves by a magnetic multilayer traversed by a current, Phys. Rev. B **54**, 9353 (1996).

[6] L. Liu, C.-F. Pai, D. C. Ralph, and R. A. Buhrman, Magnetic Oscillations Driven by the Spin Hall Effect in 3-Terminal

Magnetic Tunnel Junction Devices, Phys. Rev. Lett. **109**, 186602 (2012).

[7] L. Liu, O. J. Lee, T. J. Gudmundsen, D. C. Ralph, and R. A. Buhrman, Current-Induced Switching of Perpendicularly Magnetized Magnetic Layers Using Spin Torque from the Spin Hall Effect, Phys. Rev. Lett. **109**, 096602 (2012).

[8] L. Liu, C.-F. Pai, Y. Li, H. W. Tseng, D. C. Ralph, and R. A. Buhrman, Spin-torque switching with the giant spin Hall effect of tantalum, Science **336**, 555 (2012).

[9] C.-F. Pai, L. Liu, Y. Li, H. W. Tseng, D. C. Ralph, and R. A. Buhrman, Spin transfer torque devices utilizing the giant spin Hall effect of tungsten, Appl. Phys. Lett. **101**, 122404 (2012).

[10] M. Cubukcu, O. Boulle, M. Drouard, K. Garello, C. O. Avci, I. M. Miron, J. Langer, B. Ocker, P. Gambardella, and G. Gaudin, Spin-orbit torque magnetization switching of a three-terminal perpendicular magnetic tunnel junction, Appl. Phys. Lett. **104**, 042406 (2014).

[11] G. Yu, P. Upadhyaya, Y. Fan, J. G. Alzate, W. Jiang, K. L. Wong, S. Takei, S. A. Bender, L.-T. Chang, Y. Jiang, M. Lang, J. Tang, Y. Wang, Y. Tserkovnyak, P. K. Amiri, and K. L. Wang, Switching of a perpendicular magnetization by spin-orbit torques in the absence of external magnetic fields, Nat. Nanotechnol. **9**, 548 (2014).

[12] L. You, O. L. nd D. Bhowmik, D. Labanowski, J. Hong, J. Bokor, and S. Salahuddin, Switching of perpendicularly polarized nanomagnets with spin orbit torque without an external magnetic field by engineering a tilted anisotropy, Proc. Natl. Acad. Sci. **112**, 10310 (2015).

[13] J. Torrejon, F. Garcia-Sanchez, T. Taniguchi, J. Sinha, S. Mitani, J.-V. Kim, and M. Hayashi, Current-driven asymmetric magnetization switching in perpendicularly magnetized CoFeB/MgO heterostructures, Phys. Rev. B **91**, 214434 (2015).

[14] S. Fukami, T. Anekawa, C. Zhang, and H. Ohno, Magnetization switching by spin-orbit torque in an antiferromagnet-ferromagnet bilayer system, Nat. Mater. **15**, 535 (2016).

[15] Y.-W. Oh, S. h. C. Baek, Y. M. Kim, H. Y. Lee, K.-D. Lee, C.-G. Yang, E.-S. Park, K.-S. Lee, K.-W. Kim, G. Go, J.-R. Jeong, B.-C. Min, H.-W. Lee, K.-J. Lee, and B.-G. Park, Field-free switching of perpendicular magnetization through spin-orbit torque in antiferromagnet/ferromagnet/oxide structures, Nat. Nanotechnol. **11**, 878 (2016).

[16] A. van den Brink, G. Vermijs, A. Solignac, J. Koo, J. T. Kohlhepp, H. J. M. Swagten, and B. Koopmans, Field-free magnetization reversal by spin-Hall effect and exchange bias, Nat. Commun. **7**, 10854 (2016).

[17] Y.-C. Lau, D. Betto, K. Rode, J. M. D. Coey, and P. Stamenov, Spin-orbit torque switching without an external field using interlayer exchange coupling, Nat. Nanotechnol. **11**, 758 (2016).

[18] S. Fukami, T. Anekawa, C. Zhang, and H. Ohno, A spin-orbit torque switching scheme with collinear magnetic easy axis and current configuration, Nat. Nanotechnol. **11**, 621 (2016).

[19] G. Bertotti, I. Mayergoyz, and C. Serpico, *Nonlinear Magnetization Dynamics in Nanosystems* (Elsevier, Amsterdam, 2009).

[20] B. Dieny, R. B. Goldfarb, and K.-J. Lee (Eds.), *Introduction to Magnetic Random-Access Memory* (Wiley-IEEE, Hoboken, NJ, 2016).

[21] J. A. Katine, F. J. Albert, R. A. Buhrman, E. B. Myers, and D. C. Ralph, Current-Driven Magnetization Reversal and Spin-Wave Excitations in Co/Cu/Co Pillars, Phys. Rev. Lett. **84**, 3149 (2000).

[22] S. I. Kiselev, J. C. Sankey, I. N. Krivorotov, N. C. Emley, R. J. Schoelkopf, R. A. Buhrman, and D. C. Ralph, Microwave oscillations of a nanomagnet driven by a spin-polarized current, Nature (London) **425**, 380 (2003).

[23] J. Z. Sun, Spin-current interaction with a monodomain magnetic body: A model study, Phys. Rev. B **62**, 570 (2000).

[24] J. Grollier, V. Cros, H. Jaffrés, A. Hamzic, J. M. George, G. Faini, J. B. Youssef, H. LeGall, and A. Fert, Field dependence of magnetization reversal by spin transfer, Phys. Rev. B **67**, 174402 (2003).

[25] H. Kubota, A. Fukushima, Y. Ootani, S. Yuasa, K. Ando, H. Maehara, K. Tsunekawa, D. D. Djayaprawira, N. Watanabe, and Y. Suzuki, Evaluation of spin-transfer switching in Ce-FeB/MgO/CoFeB magnetic tunnel junctions, Jpn. J. Appl. Phys. **44**, L1237 (2005).

[26] J. Kim, J. Sinha, M. Hayashi, M. Yamanouchi, S. Fukami, T. Suzuki, S. Mitani, and H. Ohno, Layer thickness dependence of the current-induced effective field vector in Ta| CoFeB| MgO, Nat. Mater. **12**, 240 (2012).

[27] J. Kim, P. Sheng, S. Takahashi, S. Mitani, and M. Hayashi, Spin Hall Magnetoresistance in Metallic Bilayers, Phys. Rev. Lett. **116**, 097201 (2016).

[28] K.-S. Lee, S.-W. Lee, B.-C. Min, and K.-J. Lee, Theoretical Current for Switching of a Perpendicular Magnetic Layer Induced by Spin Hall Effect, Appl. Phys. Lett. **102**, 112410 (2013).

[29] K.-S. Lee, S.-W. Lee, B.-C. Min, and K.-J. Lee, Thermally activated switching of perpendicular magnet by spin-orbit spin torque, J. Appl. Phys. **104**, 072413 (2014).

[30] T. Taniguchi, Nonlinear analysis of magnetization dynamics excited by spin Hall effect, Phys. Rev. B **91**, 104406 (2015).

[31] T. Taniguchi, S. Mitani, and M. Hayashi, Critical current destabilizing perpendicular magnetization by the spin Hall effect, Phys. Rev. B **92**, 024428 (2015).

[32] T. Taniguchi, Theoretical condition for switching the magnetization in a perpendicularly magnetized ferromagnet via the spin Hall effect, Phys. Rev. B **100**, 174419 (2019).

[33] D.-K. Lee and K.-J. Lee, Spin-orbit torque switching of perpendicular magnetization in ferromagnetic trilayers, Sci. Rep. **10**, 1772 (2020).

[34] D. Zhu and W. Zhao, Threshold current density for perpendicular magnetization switching through spin-orbit torque, Phys. Rev. Appl. **13**, 044078 (2020).

[35] J. Z. Sun, R. P. Robertazzi, J. Nowak, P. L. Trouilloud, G. Hu, D. W. Abraham, M. C. Gaidis, S. L. Brown, E. J. O'Sullivan, W. J. Gallagher, and D. C. Worledge, Effect of subvolume excitation and spin-torque efficiency on magnetic switching, Phys. Rev. B **84**, 064413 (2011).

[36] G. D. Chaves-O'Flynn, E. V. Eijnden, D. L. Stein, and A. D. Kent, Energy barriers to magnetization reversal in perpendicularly magnetized thin film nanomagnets, J. Appl. Phys. **113**, 023912 (2013).

[37] G. D. Chaves-O'Flynn, G. Wolf, J. Z. Sun, and A. D. Kent, Thermal stability of magnetic states in circular thin-film nanomagnets with large perpendicular magnetic anisotropy, Phys. Rev. Appl. **4**, 024010 (2015).

[38] Y. Suzuki, A. A. Tulapurkar, and C. Chappert, in *Nanomagnetism and Spintronics*, edited by T. Shinjo (Elsevier, Amsterdam, 2009), Chap. 3.

[39] W. F. Brown, Jr., Thermal fluctuations of a single-domain particle, Phys. Rev. **130**, 1677 (1963).

[40] E. B. Myers, F. J. Albert, J. C. Sankey, E. Bonet, R. A. Buhrman, and D. C. Ralph, Thermally Activated Magnetic Reversal Induced by a Spin-Polarized Current, Phys. Rev. Lett. **89**, 196801 (2002).

[41] R. H. Koch, J. A. Katine, and J. Z. Sun, Time-Resolved Reversal of Spin-Transfer Switching in a Nanomagnet, Phys. Rev. Lett. **92**, 088302 (2004).

[42] D. M. Apalkov and P. B. Visscher, Spin-torque switching: Fokker-Planck rate calculation, Phys. Rev. B **72**, 180405(R) (2005).

[43] D. Bedau, H. Liu, J. Z. Sun, J. A. Katine, E. E. Fullerton, S. Mangin, and A. D. Kent, Spin-transfer pulse switching: From the dynamic to the thermally activated regime, Appl. Phys. Lett. **97**, 262502 (2010).

[44] T. Taniguchi and H. Imamura, Thermally assisted spin transfer torque switching in synthetic free layers, Phys. Rev. B **83**, 054432 (2011).

[45] W. H. Butler, T. Mewes, C. K. A. Mewes, P. B. Visscher, W. H. Rippard, S. E. Russek, and R. Heindl, Switching distribution for perpendicular spin-torque devices within the macrospin approximation, IEEE Trans. Magn. **48**, 4684 (2012).

[46] T. Taniguchi and H. Imamura, Thermal switching rate of a ferromagnetic material with uniaxial anisotropy, Phys. Rev. B **85**, 184403 (2012).

[47] H. Sato, M. Yamanouchi, S. Ikeda, S. Fukami, F. Matsukura, and H. Ohno, Perpendicular-anisotropy CoFeB-MgO magnetic tunnel junctions with a MgO/CoFeB/Ta/CoFeB/MgO recording structure, Appl. Phys. Lett. **101**, 022414 (2012).

[48] T. Taniguchi, M. Shibata, M. Marthaler, Y. Utsumi, and H. Imamura, Numerical study on spin torque switching in thermally activated region, Appl. Phys. Express **5**, 063009 (2012).

[49] K. A. Newhall and E. Vanden-Eijnden, Averaged equation for energy diffusion on a graph reveals bifurcation diagram and thermally assisted reversal times in spin-torque driven nanomagnets, J. Appl. Phys. **113**, 184105 (2013).

[50] H. Tomita, S. Miwa, T. Nozaki, S. Yamashita, T. Nagase, K. Nishiyama, E. Kitagawa, M. Yoshikawa, T. Daibou, M. Nagamine, T. Kishi, S. Ikegawa, N. Shimomura, H. Yoda, and Y. Suzuki, Unified understanding of both thermally assisted and precessional spin-transfer switching in perpendicularly magnetized giant magnetoresistive nanopillars, Appl. Phys. Lett. **102**, 042409 (2013).

[51] T. Taniguchi, Y. Utsumi, M. Marthaler, D. S. Golubev, and H. Imamura, Spin torque switching of an in-plane magnetized system in a thermally activated region, Phys. Rev. B **87**, 054406 (2013).

[52] D. B. Gopman, D. Bedau, S. Mangin, E. E. Fullerton, J. A. Katine, and A. D. Kent, Switching field distribution with spin transfer torques in perpendicularly magnetized spin-valve nanopillars, Phys. Rev. B **89**, 134427 (2014).

[53] S. Yakata, H. Kubota, Y. Suzuki, K. Yakushiji, A. Fukushima, S. Yuasa, and K. Ando, Influence of perpendicular magnetic anisotropy on spin-transfer switching current in CoFeB/MgO/CoFeB magnetic tunnel junctions, J. Appl. Phys. **105**, 07D131 (2009).

[54] S. Ikeda, K. Miura, H. Yamamoto, K. Mizunuma, H. D. Gan, M. Endo, S. Kanai, J. Hayakawa, F. Matsukura, and H. Ohno, A perpendicular-anisotropy CoFeB-MgO magnetic tunnel junction, Nat. Mater. **9**, 721 (2010).

[55] H. Kubota, S. Ishibashi, T. Saruya, T. Nozaki, A. Fukushima, K. Yakushiji, K. Ando, Y. Suzuki, and S. Yuasa, Enhancement of perpendicular magnetic anisotropy in FeB free layers using a thin MgO cap layer, J. Appl. Phys. **111**, 07C723 (2012).

[56] M. Oogane, T. Wakitani, S. Yakata, R. Yilgin, Y. Ando, A. Sakuma, and T. Miyazaki, Magnetic damping in ferromagnetic thin films, Jpn. J. Appl. Phys. **45**, 3889 (2006).

[57] T. Taniguchi and H. Kubota, Spin torque oscillator for microwave assisted magnetization reversal, Jpn. J. Appl. Phys. **57**, 053001 (2018).